FRONTIERS OF PHYSICS

RESEARCH ARTICLE
Volume 18 / Issue 5 / 52307 / 2023

Measurement of interacting quantum phases: A band mapping scheme

Qi Huang[1,†], Zijie Zhu[2], Yifei Wang[3], Libo Liang[1], Qinpei Zheng[1], Xuzong Chen[1,‡]

1 School of Electronics, Peking University, Beijing 100871, China
2 Institute for Quantum Electronics, ETH Zürich, 8093 Zürich, Switzerland
3 Institute for Advanced Study, Tsinghua University, Beijing 100084, China
Corresponding authors. E-mail: †qihuang@pku.edu.cn, ‡xuzongchen@pku.edu.cn
Received June 13, 2023; accepted June 20, 2023

ABSTRACT

Band mapping is widely used in various scenarios of cold atom physics to measure the quasi-momentum distribution and band population. However, conventional methods fail in strongly interacting systems. Here we propose and experimentally realize a novel scheme of band mapping that can accurately measure the quasi-momentum of interacting many-body systems. Through an anisotropic control in turning down the three-dimensional optical lattice, we can eliminate the effect of interactions on the band mapping process. Then, based on a precise measurement of the quasi-momentum distribution, we introduce the incoherent fraction as a physical quantity that can quantify the degree of incoherence of quantum many-body states. This method enables precise measurement of processes such as the superfluid to Mott insulator phase transition. Additionally, by analyzing the spatial correlation derived from the quasi-momentum of superfluid-Mott insulator phase transitions, we obtain results consistent with the incoherent fraction. Our scheme broadens the scope of band mapping and provides a method for studying quantum many-body problems.

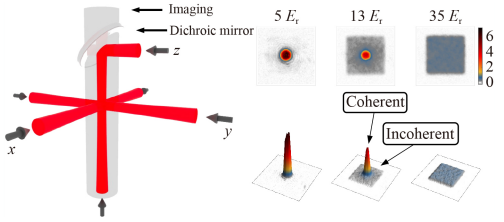

Keywords ultracold physics, Mott insulator, superfluid, band mapping

1 Introduction

Band mapping [1, 2] is a powerful method for probing the quasi-momentum distribution [3, 4] and band occupation [5–8] of quantum systems in ultracold atomic physics. This method has been widely applied to reveal the quantum properties of various quantum phases [3, 4, 6–8], nonequilibrium dynamics [9], topological invariants [10–17] and topological quantum dynamics [18–20]. By applying lattice modulation [21–24] to excite the system, band mapping can measure the population of different bands [25–27] or sublattices [28–34] in complex lattice geometries. Band mapping can also be combined with photoemission spectroscopy and quantum gas microscopy to access the spectral functions with quantum gas microscopy [35]. Site-resolved band mapping is also available [32].

The conventional band mapping method has enabled the measurement of band populations, quasi-momentum, topology, and even *in situ* imaging in systems with weak or negligible interactions. However, for interacting systems, especially strongly interacting ones, the conventional band mapping method fails to accurately measure the quasi-momentum distribution because the interactions can modify the quasi-momentum distribution during the ramping down process that transforms the quasi-momen-

Higher Education Press

https://doi.org/10.1007/s11467-023-1326-y

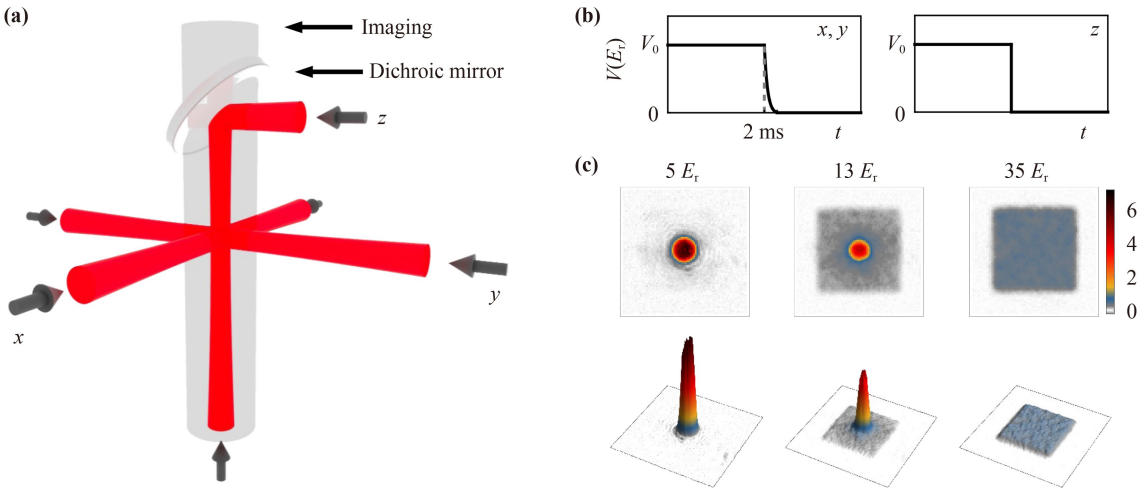

Fig. 1 Sketch of experiment setup, time sequence, and images for band mapping. **(a)** A schematic diagram of the experimental system. **(b)** The temporal sequence of the lattice potential along the x, y, and z directions. The potential along the x and y directions is ramped down to zero within 2 ms, while the potential along the z direction is abruptly quenched to zero. **(c)** We obtained band mapping images with our method at three different lattice depths corresponding to the superfluid regime, the critical point of phase transition, and the deep Mott insulator regime.

tum distribution into momentum distribution in free space [36]. Consequently, even the superfluid (SF) to Mott insulator (MI) transition in three-dimensional (3D) optical lattices has not been observed accurately in terms of quasi-momentum measurement.

In this work, we experimentally developed a novel band mapping scheme for probing interacting quantum systems in a three-dimensional optical lattice with high precision. Our main idea is to introduce a new ramping process for band mapping, which eliminates the influence caused by interactions in experimental detection. As a result, in sharp contrast to the conventional band mapping method, which is suitable for non-interacting or weakly interacting systems, our scheme preserves the quasi-momentum distribution of the many-body state during the ramping down process. We apply our scheme to the SF to MI phase transition and measure the quasi-momentum distribution of both phases reliably. Based on the accurate quasi-momentum distribution, we introduce two quantum phase measures, incoherent fraction and spatial correlation function, to experimentally distinguish SF and MI phases. Our scheme may pave a way to investigate strongly interacting cold atom systems based on the band mapping method.

2 Improved band mapping method

We perform experiments with ultracold ^{87}Rb atoms in 3D optical lattices to demonstrate the reliability of an improved band mapping method in an interacting regime. Figure 1(a) shows a schematic diagram of our experimental system. The 3D cubic optical lattice is formed by superimposing standing waves perpendicularly to each other with orthogonal polarizations and different frequencies, each having a wavelength of around $\lambda \approx 1064\,\mathrm{nm}$. The system is described by the Bose–Hubbard model, with the Hamiltonian [37]:

$$\hat{H} = -J\sum_{\langle i,j\rangle}\hat{a}_i^\dagger\hat{a}_j + \frac{U}{2}\sum_i \hat{n}_i\left(\hat{n}_i - 1\right) - \sum_i\left(\mu - \frac{1}{2}m\omega_0^2 r_i^2\right)\hat{n}_i, \quad (1)$$

where $\hat{a}_i^\dagger$ ($\hat{a}_i$) creates (annihilates) a boson at site i, $\langle i,j\rangle$ denotes nearest-neighbor sites and $\hat{n}_i = \hat{a}_i^\dagger\hat{a}_i$ is the number operator. The parameters J, U and μ represent the tunneling coefficient, on-site interaction, and the chemical potential, respectively, and are controlled by the potential depth of the optical lattice. The last term accounts for the harmonic confining potential with atomic mass m and frequency ω_0.

The conventional band mapping method for single-particle or weak interaction regime encounters severe difficulties when extended to the interacting regime. The crucial step of band mapping is the ramping procedure of lattice potential. The duration of ramping process Δt is constrained by two characteristic time scales $\tau_1 \ll \Delta t \ll \tau_2$. The ramping is slow with respect to the band gap, where $\tau_1 \sim 0.1\,\mathrm{ms}$ is the characteristic time required for the quasi-momentum to adiabatically evolve into momentum, and τ_2 is the time over which the quasi-momentum occupation remains unchanged. τ_2 generically scales as h/U and $1/\nu$, where h is the Planck constant, ν is the trap frequency trap. For the non-interacting or weak interacting regime, $\tau_2 > 10\,\mathrm{ms}$ and it is easy to choose an appropriate Δt. However, τ_2 is greatly reduced

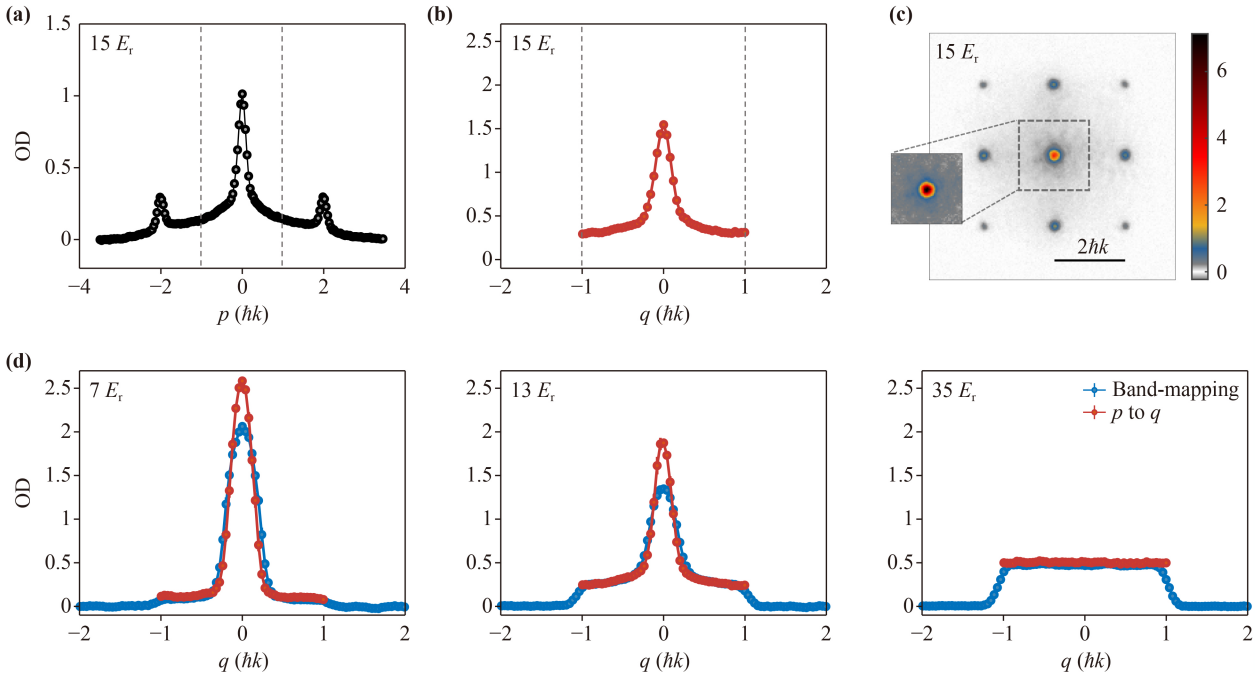

Fig. 2 Quasi-momentum distribution from two methods. **(a)** Integration graphs of (c) along the x axis. **(b)** Quasi-momentum distribution is calculated from the first Brillouin zone of (a). **(c)** The integrated column density $n(x, y)$, represented by the optical density (OD) in arbitrary units, is measured from the experiment at $15\,E_r$. The inset shows the quasi-momentum obtained from the first Brillouin zone of momentum distribution. **(d)** Integrated graphs of band mapping at different lattice depths. Red points represent quasi-momentum distribution calculated from momentum distribution, while blue points represent the data obtained from the new band mapping method. Experimental data are averaged over several realizations. Error bars denote standard deviation; most error bars are smaller than their marker size if not visible.

by the interaction $\tau \sim h/U \sim 1\,\text{ms}$, making it challenging to determine Δt.

Here, we propose a novel ramping process for band mapping. For a 3D system, we ramp down the optical potentials of x and y directions over 2 ms and quench optical potential of z direction to zero, as shown in Fig. 1(b). This contrasts with the ramping process in the conventional band mapping method, where the lattice potentials in each direction are simultaneously ramped down, which inevitably involves interactions and decreases τ_2. Our method, however, circumvents this problem. This is achieved by quenching the lattice potential of the z direction to zero, so that the interactions are released along the z direction, and the system can be regarded as a (nearly) non-interacting system. As a result, τ_2 is restored to a large value and band mapping works. It is worth noting that this ramping process allows us to probe the quasi-momentum population along the x and y directions since our imaging system is along the z direction, so quenching the potential of the z direction preserves the information along the x and y directions. After 30 ms time of flight (TOF) absorption imaging was performed, the quasi-momentum information in the x and y directions of the many-body state can be feasibly obtained.

The novel scheme of band mapping enables us to measure the quasi-momentum distribution of the SF to MI phase transition. We measured the quasi-momentum distribution of the atoms in the optical lattice for different values of the lattice depth V_0. Figure 1(c) displays the results for $V_0 = 5\,E_r$, $13\,E_r$, and $35\,E_r$, where $E_r = \hbar^2 k^2/(2m)$ is the recoil energy, $k = 2\pi/\lambda$ is the wave vector and $\hbar$ is the reduced Planck constant. When $V_0 = 5\,E_r$, the quasi-momentum shows a coherent peak around $q = 0$, as expected for the SF phase. As V_0 increases, the coherence peak decreases continuously and the plateau gradually rises. In the limit of $J/U \to 0$, the system enters a deep MI phase and exhibits a flat quasi-momentum distribution. This contrasts with the results obtained by the conventional band mapping method (see Appendix A), which is affected by strong interactions in the MI phase and fails to detect the intrinsic quasi-momentum. Our method reveals the quantum phase transition from SF to MI with high fidelity.

3 Derivation of quasi-momentum distribution from momentum distribution

Before proceeding to investigate the many-body quantum phases with precisely measured quasi-momentum, we introduce another method to extract the quasi-momentum

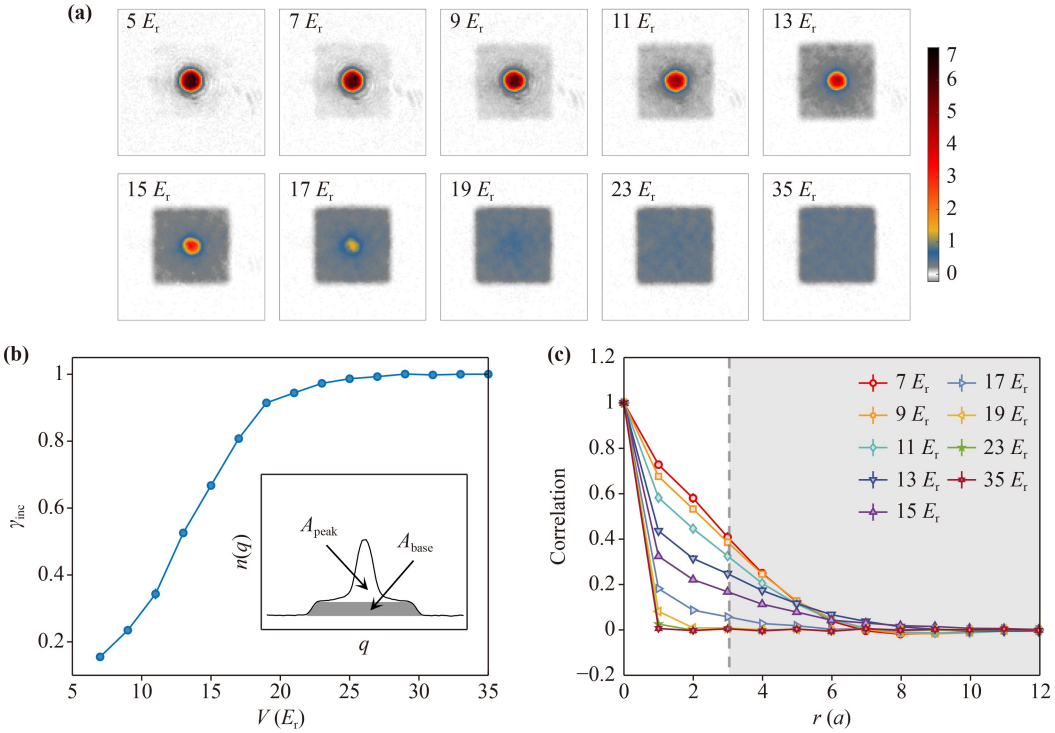

Fig. 3 Incoherent fraction and correlation. **(a)** Band mapping images reveal the quasi-momentum distribution at various lattice depths, showing a transition from SF to MI as indicated by the diminishing peak and the increasing plateau. **(b)** Lattice depth dependence of the incoherent fraction. The inset depicts the method for extracting the incoherent fraction from the quasi-momentum distribution. **(c)** Correlation versus space distance at different lattice depths. The gray area has errors due to inhomogeneous optical lattice.

distribution from the conventional TOF technique, which is qualitatively consistent with our new band mapping method and validates the experiment. The momentum can be obtained from the TOF imaging, and the quasi-momentum can be obtained by

$$\langle \hat{a}_p^\dagger \hat{a}_p \rangle = \langle q|p\rangle\langle p|q\rangle \cdot \langle \hat{a}_q^\dagger \hat{a}_q \rangle , \tag{2}$$

if we assume only the lowest energy band is considered. Here $\hat{a}_p^\dagger$ ($\hat{a}_p$) creates (annihilates) a boson with momentum p, and $\hat{a}_q^\dagger$ ($\hat{a}_q$) creates (annihilates) a boson with quasi-momentum q. Notice that q is in the first Brillouin zone, q and p differ by an integer multiple of $\hbar b$, where b is the smallest reciprocal lattice vector.

Figure 2 compares the quasi-momentum distribution obtained by two methods. In the upper panel, Fig. 2(a) shows the integrated momentum distribution from the raw data in Fig. 2(c) by integrating along the x axis, and Fig. 2(b) shows the quasi-momentum distribution that was calculated based on Fig. 2(a) according to Eq. (2). The lower panel shows the quasi-momentum distribution from both methods at several values of the lattice potential V_0. The two methods show a good qualitative agreement. The slight difference between the distributions obtained from two methods is partly due to the inhomogeneous lattice formed by the Gaussian beam. We note that the edge of the flat quasi-momentum plateau drops smoothly to zero, rather than abruptly, because the edge of the band cannot be perfectly adiabatic and the resolution of the imaging system can not exhibit completely vertical edges.

4 Characterization of quantum state coherence

In this section, we introduce two physical quantities that characterize quantum many-body states, which can be accessed by the accurate quasi-momentum distribution. The two methods can accurately measure phase transitions from the perspectives of momentum space and real space, respectively, and the two methods are mutually consistent.

4.1 Incoherent fraction

We employ the incoherent fraction to quantify the degree of incoherence of any quantum state. By precisely measuring the quasi-momentum distribution, which can be divided into two components, we can identify the coherent part as the peak and the incoherent part as the plateau, as shown in Fig. 3(a), the incoherent fraction γ_{inc} is given by

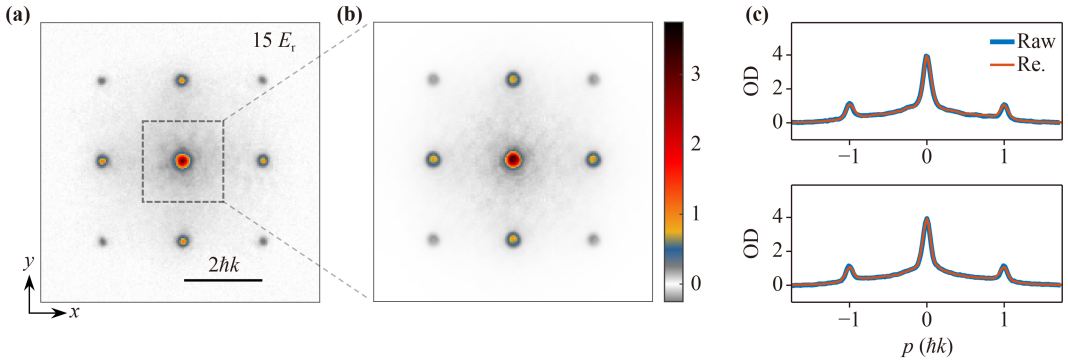

Fig. 4 Transformation of momentum distribution between different Brillouin zones. **(a)** The momentum distribution in an optical lattice with a potential depth of $15\,E_r$. **(b)** By extrapolating the momentum distribution within the first Brillouin zone, we derived the complete momentum distribution. **(c)** We integrated (a) and (b) along the x and y directions, shown as blue and orange lines, respectively.

$$\gamma_{\text{inc}} = \frac{A_{\text{base}}}{A_{\text{total}}} = 1 - \frac{A_{\text{peak}}}{A_{\text{total}}}, \tag{3}$$

the peak and plateau parts are represented by A_{peak} and A_{base}, respectively, as shown in the inset of Fig. 3(b), which is the integrated image of the experimental column density [Fig. 3(a)] along one direction, where the gray area is A_{base}, the area above the gray part represents A_{peak}, and the height of the gray part is $n\,(q \sim \pm\hbar k)$, with $A_{\text{total}} = A_{\text{peak}} + A_{\text{base}}$.

The incoherent fraction quantifies the superfluid to Mott insulator phase transition in inhomogeneous systems, as indicated in Fig. 3(b). Figure 3(b) shows γ_{inc} as a function of lattice potential. When the system is in the SF regime, γ_{inc} has a relatively small value, suggesting that most of the atoms remain phase coherent in the SF phase. As the lattice potential increases, the system transitions to the MI regime, and γ_{inc} increases, reflecting the localization of atoms and the decrease of coherence. For the deep Mott regime, the γ_{inc} saturates to a value near 1 as expected.

4.2 Spatial correlation function

Spatial correlation function $C_{\text{SF}}(i,j)$ distinguishes the SF phase and the MI phase by means of their decay behavior. With the quasi-momentum distribution measured from the new band mapping scheme, $C_{\text{SF}}(i,j)$ can be evaluated by

$$C_{\text{SF}}(i,j) = \left\langle \hat{a}_i^\dagger \hat{a}_j \right\rangle = \frac{1}{N} \sum_{q \in \text{BZ}} \mathrm{e}^{-\mathrm{i}\frac{q}{\hbar}(x_i - x_j)} \left\langle \hat{a}_q^\dagger \hat{a}_q \right\rangle, \tag{4}$$

where $\hat{a}_q^\dagger$ ($\hat{a}_q$) creates (annihilates) a boson with quasi-momentum q. Given that the system has a background harmonic trap potential, Eq. (4) applies within the range of the characteristic length $l_\omega = \sqrt{\hbar/(m\omega_0)}$. Using the deepest lattice potential $35\,E_r$ and the largest envelope potential frequency $\omega_0 \approx 60\,\text{Hz} \times 2\pi$, we can estimate the minimum characteristic length $l_\omega \sim 3a$ in the experimental data, where $a \approx 532\,\text{nm}$ is the lattice constant. Therefore in our work, we focus on the short-distance behavior of C_{SF}, which still displays qualitatively distinct decays for different quantum phases.

Figure 3(c) shows the distinct decay behavior of $C_{\text{SF}}(i,j)$ as a function of spatial distance $r = x_i - x_j$ for different lattice potentials V_0. In the SF regime ($V_0 \leqslant 11\,E_r$), $C_{\text{SF}}(i,j)$ decays nearly linearly over short distances ($1 < r \leqslant 3a$). On the other hand, $C_{\text{SF}}(i,j)$ decays rather quickly after crossing the phase transition point ($\sim 13\,E_r$). When $V_0 > 23\,E_r$, the system enters a deep MI regime, and $C_{\text{SF}}(i,j)$ rapidly decreases to 0.

The observations above are in good agreement with the incoherent fraction γ_{inc}. The decreasing trend of the correlation is consistent with the incoherent fraction, and the correlation tends to 0 as the incoherent fraction tends to 1. The incoherent fraction and spatial correlation provide information from momentum space and real space, respectively. They are consistent with each other and enable precise determination of the phase transition.

5 Transformation of momentum distribution between different Brillouin zones

In addition to deriving the quasi-momentum distribution from the momentum distribution, we also find that the full momentum distribution can be reconstructed from the momentum distribution of the first Brillouin zone for relatively flat optical lattices, namely,

$$\frac{\left\langle \hat{a}_{p'}^\dagger \hat{a}_{p'} \right\rangle}{\left\langle \hat{a}_p^\dagger \hat{a}_p \right\rangle} = \frac{|\langle p'|q\rangle|^2}{|\langle p|q\rangle|^2}, \tag{5}$$

where p is the momentum in the first Brillouin zone. p' is any momentum in an arbitrary Brillouin zone. q represents quasi-momentum. Figure 4(a) shows the raw

data for the $15\,E_r$ case, Fig. 4(b) shows the reconstruction from the first Brillouin zone of Fig. 4(a), and Fig. 4(c) compares their integrations along the x and y directions. The blue and orange curves represent the raw and reconstructed data, respectively, and agree well with each other. This method can be used to assess whether the imaging is saturated. The saturation of the main peak leads to a reduction of the transformed secondary peak compared to the original data. The size of the Brillouin zone is sufficient to reconstruct the full momentum distribution.

6 Conclusion and outlook

We experimentally developed a novel band mapping method that is demonstrated to be feasible in detecting interacting quantum phases. It offers a straightforward, fast, and effective way to perform band mapping. We investigate a 3D Bose–Hubbard model as an example. Also, we obtain an accurate quasi-momentum distribution from the new band mapping scheme, based on which, we obtain the new experimental observable the incoherent fraction γ_{inc}. The spatial correlation function derived from quasi-momentum successfully differentiates the SF and the MI phases and agrees with γ_{inc}. These two methods reveal many-body states and phase transitions from momentum space and real space, respectively, and allow for accurate measurements of phase transitions. We also show that the momentum distribution can be reconstructed from a single Brillouin zone, which can be used to assess the lattice flatness and the imaging saturation. We want to point out that the new observable γ_{inc} we propose in this work can probe both static and dynamic properties of quantum phases [9]. Combined with quantum Monte Carlo, γ_{inc} enables high-precision measurement of the temperature of ultracold atoms in optical lattices. Our band mapping method has wide applications in various cold atom systems, especially for studying many-body quantum phase transitions and dynamics.

Declarations The authors declare that they have no competing interests and there are no conflicts.

Acknowledgements We are grateful to Xiong-Jun Liu for his valuable discussions and constructive comments, as well as his critical reading of our manuscript. We also thank Xinchi Zhou for helpful comments. This work was supported by the National Key Research and Development Program of China (No. 2021YFA1400900).

Appendix A: Comparison of conventional and improved band mapping methods

Figure A1 shows the measurement results of the conventional and our novel band mapping scheme at lattice potential $V_0 = 7\,E_r$, $13\,E_r$, and $35\,E_r$. In the SF regime at $7\,E_r$, the conventional method fails to resolve a plateau. In the deep MI regime at $35\,E_r$, our method reveals a flat plateau which corresponds to a uniform distribution in the first Brillouin zone. However, the conventional method cannot detect the plateau, as shown in Fig. A1.

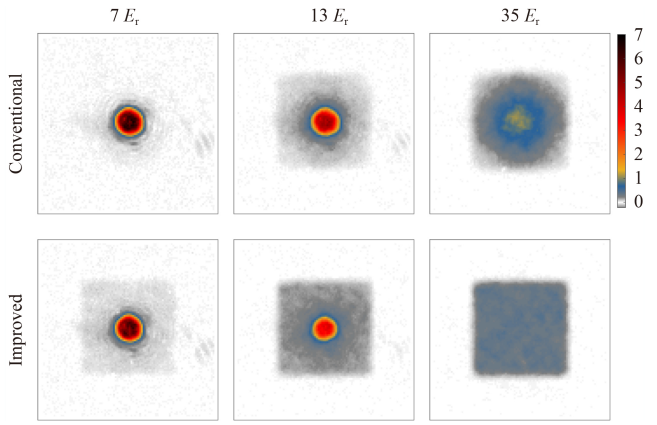

Fig. A1 Comparison of conventional method and improved band mapping at several typical lattice depths.

References

1. M. Greiner, I. Bloch, O. Mandel, T. W. Hänsch, and T. Esslinger, Exploring phase coherence in a 2D lattice of Bose–Einstein condensates, *Phys. Rev. Lett.* 87(16), 160405 (2001)
2. M. Köhl, H. Moritz, T. Stöferle, K. Günter, and T. Esslinger, Fermionic atoms in a three dimensional optical lattice: Observing Fermi surfaces, dynamics, and interactions, *Phys. Rev. Lett.* 94(8), 080403 (2005)
3. U. Schneider, L. Hackermuller, S. Will, T. Best, I. Bloch, T. A. Costi, R. Helmes, D. Rasch, and A. Rosch, Metallic and insulating phases of repulsively interacting fermions in a 3D optical lattice, *Science* 322(5907), 1520 (2008)
4. Z. A. Geiger, K. M. Fujiwara, K. Singh, R. Senaratne, S. V. Rajagopal, M. Lipatov, T. Shimasaki, R. Driben, V. V. Konotop, T. Meier, and D. M. Weld, Observation and uses of position–space Bloch oscillations in an ultracold gas, *Phys. Rev. Lett.* 120(21), 213201 (2018)
5. M. Aidelsburger, M. Atala, M. Lohse, J. T. Barreiro, B. Paredes, and I. Bloch, Realization of the Hofstadter Hamiltonian with ultracold atoms in optical lattices, *Phys. Rev. Lett.* 111(18), 185301 (2013)
6. C. J. Kennedy, W. C. Burton, W. C. Chung, and W. Ketterle, Observation of Bose–Einstein condensation in a strong synthetic magnetic field, *Nat. Phys.* 11(10), 859 (2015)
7. J. H. Kang, J. H. Han, and Y. I. Shin, Realization of a cross-linked chiral ladder with neutral fermions in a 1D optical lattice by orbital–momentum coupling, *Phys. Rev. Lett.* 121(15), 150403 (2018)
8. C. D. Brown, S. W. Chang, M. N. Schwarz, T. H.

Leung, V. Kozii, A. Avdoshkin, J. E. Moore, and D. Stamper-Kurn, Direct geometric probe of singularities in band structure, *Science* 377(6612), 1319 (2022)
9. Q. Huang, R. Yao, L. Liang, S. Wang, Q. Zheng, D. Li, W. Xiong, X. Zhou, W. Chen, X. Chen, and J. Hu, Observation of many-body quantum phase transitions beyond the Kibble–Zurek mechanism, *Phys. Rev. Lett.* 127(20), 200601 (2021)
10. L. Tarruell, D. Greif, T. Uehlinger, G. Jotzu, and T. Esslinger, Creating, moving and merging Dirac points with a Fermi gas in a tunable honeycomb lattice, *Nature* 483(7389), 302 (2012)
11. X. J. Liu, K. T. Law, T. K. Ng, and P. A. Lee, Detecting topological phases in cold atoms, *Phys. Rev. Lett.* 111(12), 120402 (2013)
12. G. Jotzu, M. Messer, R. Desbuquois, M. Lebrat, T. Uehlinger, D. Greif, and T. Esslinger, Experimental realization of the topological Haldane model with ultracold fermions, *Nature* 515(7526), 237 (2014)
13. M. Aidelsburger, M. Lohse, C. Schweizer, M. Atala, J. T. Barreiro, S. Nascimbène, N. Cooper, I. Bloch, and N. Goldman, Measuring the Chern number of Hofstadter bands with ultracold bosonic atoms, *Nat. Phys.* 11(2), 162 (2015)
14. Z. Wu, L. Zhang, W. Sun, X. T. Xu, B. Z. Wang, S. C. Ji, Y. Deng, S. Chen, X. J. Liu, and J. W. Pan, Realization of two-dimensional spin–orbit coupling for Bose–Einstein condensates, *Science* 354(6308), 83 (2016)
15. B. Song, L. Zhang, C. He, T. F. J. Poon, E. Hajiyev, S. Zhang, X. J. Liu, and G. B. Jo, Observation of symmetry-protected topological band with ultracold fermions, *Sci. Adv.* 4(2), eaao4748 (2018)
16. L. Asteria, D. T. Tran, T. Ozawa, M. Tarnowski, B. S. Rem, N. Fläschner, K. Sengstock, N. Goldman, and C. Weitenberg, Measuring quantized circular dichroism in ultracold topological matter, *Nat. Phys.* 15(5), 449 (2019)
17. Z. Y. Wang, X. C. Cheng, B. Z. Wang, J. Y. Zhang, Y. H. Lu, C. R. Yi, S. Niu, Y. Deng, X. J. Liu, S. Chen, and J. W. Pan, Realization of an ideal Weyl semimetal band in a quantum gas with 3D spin–orbit coupling, *Science* 372(6539), 271 (2021)
18. T. Li, L. Duca, M. Reitter, F. Grusdt, E. Demler, M. Endres, M. Schleier-Smith, I. Bloch, and U. Schneider, Bloch state tomography using Wilson lines, *Science* 352(6289), 1094 (2016)
19. W. Sun, C. R. Yi, B. Z. Wang, W. W. Zhang, B. C. Sanders, X. T. Xu, Z. Y. Wang, J. Schmiedmayer, Y. Deng, X. J. Liu, S. Chen, and J. W. Pan, Uncover topology by quantum quench dynamics, *Phys. Rev. Lett.* 121(25), 250403 (2018)
20. L. Zhang, L. Zhang, and X. J. Liu, Unified theory to characterize floquet topological phases by quench dynamics, *Phys. Rev. Lett.* 125(18), 183001 (2020)
21. J. Heinze, S. Götze, J. Krauser, B. Hundt, N. Fläschner, D. S. Lühmann, C. Becker, and K. Sengstock, Multiband spectroscopy of ultracold fermions: Observation of reduced tunneling in attractive Bose–Fermi mixtures, *Phys. Rev. Lett.* 107(13), 135303 (2011)
22. J. Heinze, J. Krauser, N. Fläschner, B. Hundt, S. Götze, A. Itin, L. Mathey, K. Sengstock, and C. Becker, Intrinsic photoconductivity of ultracold fermions in optical lattices, *Phys. Rev. Lett.* 110(8), 085302 (2013)
23. C. Repellin and N. Goldman, Detecting fractional Chern insulators through circular dichroism, *Phys. Rev. Lett.* 122(16), 166801 (2019)
24. S. Nakajima, N. Takei, K. Sakuma, Y. Kuno, P. Marra, and Y. Takahashi, Competition and interplay between topology and quasi-periodic disorder in thouless pumping of ultracold atoms, *Nat. Phys.* 17(7), 844 (2021)
25. B. S. Rem, N. Käming, M. Tarnowski, L. Asteria, N. Fläschner, C. Becker, K. Sengstock, and C. Weitenberg, Identifying quantum phase transitions using artificial neural networks on experimental data, *Nat. Phys.* 15(9), 917 (2019)
26. K. Singh, C. J. Fujiwara, Z. A. Geiger, E. Q. Simmons, M. Lipatov, A. Cao, P. Dotti, S. V. Rajagopal, R. Senaratne, T. Shimasaki, M. Heyl, A. Eckardt, and D. M. Weld, Quantifying and controlling prethermal nonergodicity in interacting floquet matter, *Phys. Rev. X* 9(4), 041021 (2019)
27. K. Wintersperger, C. Braun, F. N. Ünal, A. Eckardt, M. D. Liberto, N. Goldman, I. Bloch, and M. Aidelsburger, Realization of an anomalous floquet topological system with ultracold atoms, *Nat. Phys.* 16(10), 1058 (2020)
28. S. Fölling, S. Trotzky, P. Cheinet, M. Feld, R. Saers, A. Widera, T. Müller, and I. Bloch, Direct observation of second-order atom tunnelling, *Nature* 448(7157), 1029 (2007)
29. D. Greif, T. Uehlinger, G. Jotzu, L. Tarruell, and T. Esslinger, Short-range quantum magnetism of ultracold fermions in an optical lattice, *Science* 340(6138), 1307 (2013)
30. P. Hauke, M. Lewenstein, and A. Eckardt, Tomography of band insulators from quench dynamics, *Phys. Rev. Lett.* 113(4), 045303 (2014)
31. S. Taie, H. Ozawa, T. Ichinose, T. Nishio, S. Nakajima, and Y. Takahashi, Coherent driving and freezing of bosonic matter wave in an optical Lieb lattice, *Sci. Adv.* 1(10), e1500854 (2015)
32. M. Lohse, C. Schweizer, H. M. Price, O. Zilberberg, and I. Bloch, Exploring 4D quantum hall physics with a 2D topological charge pump, *Nature* 553(7686), 55 (2018)
33. M. Tarnowski, F. N. Ünal, N. Fläschner, B. S. Rem, A. Eckardt, K. Sengstock, and C. Weitenberg, Measuring topology from dynamics by obtaining the Chern number from a linking number, *Nat. Commun.* 10(1), 1728 (2019)
34. S. Taie, T. Ichinose, H. Ozawa, and Y. Takahashi, Spatial adiabatic passage of massive quantum particles in an optical Lieb lattice, *Nat. Commun.* 11(1), 257 (2020)
35. P. T. Brown, E. Guardado-Sanchez, B. M. Spar, E. W. Huang, T. P. Devereaux, and W. S. Bakr, Angle-resolved photoemission spectroscopy of a Fermi–Hubbard system, *Nat. Phys.* 16(1), 26 (2020)
36. S. S. Natu, D. C. McKay, B. DeMarco, and E. J. Mueller, Evolution of condensate fraction during rapid lattice ramps, *Phys. Rev. A* 85(6), 061601 (2012)
37. M. P. Fisher, P. B. Weichman, G. Grinstein, and D. S. Fisher, Boson localization and the superfluid–insulator transition, *Phys. Rev. B* 40(1), 546 (1989)